Handheld volumetric manual compression-based quantitative micro-elastography

Qi Fang[1,2,*] | Luke Frewer[1,2] | Renate Zilkens[1,3] | Brooke Krajancich[1,2,4] | Andrea Curatolo[1,2,5] | Lixin Chin[1,2] | Kelly Y. Foo[1,2] | Devina D. Lakhiani[1,2] | Rowan W. Sanderson[1,2] | Philip Wijesinghe[1,2,6] | James D. Anstie[1,2] | Benjamin F. Dessauvagie[7,8] | Bruce Latham[7,9] | Christobel M. Saunders[3,10,11] | and Brendan F. Kennedy[1,2,12]

[1] BRITElab, Harry Perkins Institute of Medical Research, QEII Medical Centre, Nedlands and Centre for Medical Research, The University of Western Australia, Crawley, Western Australia, 6009, Australia

[2] Department of Electrical, Electronic & Computer Engineering, School of Engineering, The University of Western Australia, Crawley, Western Australia, 6009, Australia

[3] Division of Surgery, Medical School, The University of Western Australia, Crawley, Western Australia, 6009, Australia

[4] Currently with Department of Electrical Engineering, Stanford University, Stanford, USA

[5] Currently with Visual Optics and Biophotonics Group, Instituto de Óptica "Daza de Valdés", Consejo Superior de Investigaciones Cientificas (IO, CSIC), C/ Serrano, 121, Madrid, Spain

[6] Currently with SUPA, School of Physics and Astronomy, University of St Andrews, North Haugh, St Andrews, UK

[7] PathWest, Fiona Stanley Hospital, 11 Robin Warren Drive, Murdoch, Western Australia, 6150, Australia

[8] School of Pathology and Laboratory Medicine, The University of Western Australia, Crawley, Western Australia, 6009, Australia

[9] The University of Notre Dame, Fremantle, Western Australia, 6160, Australia

[10] Breast Centre, Fiona Stanley Hospital, 11 Robin Warren Drive, Murdoch, Western Australia, 6150, Australia

[11] Breast Clinic, Royal Perth Hospital, 197 Wellington Street, Perth, Western Australia, 6000, Australia

[12] Australian Research Council Centre for Personalised Therapeutics Technologies, Australia

*** Correspondence**

Qi Fang, BRITElab, Harry Perkins Institute of Medical Research, QEII Medical Centre, 6 Verdun Street, Nedlands, Western Australia, 6009, Australia

Email: qi.fang@uwa.edu.au

Compression optical coherence elastography typically requires a mechanical actuator to impart a controlled uniform strain to the sample. However, for handheld scanning, this adds complexity to the design of the probe and the actuator stroke limits the amount of strain that can be applied. In this work, we present a new volumetric imaging approach that utilises bidirectional manual compression via the natural motion of the user's hand to induce strain to the sample, realising compact, actuator-free, handheld compression optical coherence elastography. In this way, we are able to demonstrate rapid acquisition of three-dimensional quantitative micro-elastography (QME) datasets of a tissue volume (6 × 6 × 1 mm) in 3.4 seconds. We characterise the elasticity sensitivity of this freehand manual compression approach using a homogeneous silicone phantom and demonstrate comparable performance to a bench-top mounted, actuator-based approach. In addition, we demonstrate handheld volumetric manual compression-based QME on a tissue-mimicking phantom with an embedded stiff inclusion and on freshly excised human breast specimens from both mastectomy and wide local excision surgeries. Tissue results are co-registered with post-operative histology, verifying the capability of our approach to measure the elasticity of tissue and to distinguish stiff tumor from surrounding soft benign tissue.

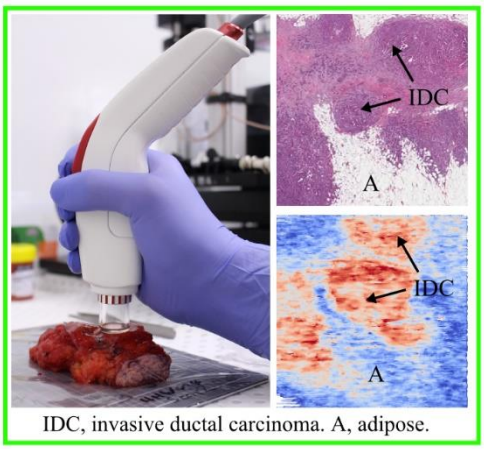

IDC, invasive ductal carcinoma. A, adipose.

KEYWORDS

freehand volumetric imaging, handheld probe, optical coherence elastography, optical coherence tomography, quantitative micro-elastography

1 | INTRODUCTION

Optical coherence elastography (OCE) [1, 2] is an emerging imaging modality that combines optical coherence tomography (OCT) [3, 4] and a loading mechanism to measure tissue mechanical properties on the micro-scale. A range of OCE techniques have been developed that can be classified based on the loading mechanism used, e.g., compression, transient and harmonic loading [5]. In compression OCE, a quasi-static mechanical loading is introduced to the tissue, typically using a piezoelectric actuator, and three-dimensional (3-D) axial strain maps of the tissue are measured [6-8]. An advantage of compression OCE, relative to other approaches, is that it can acquire large field-of-view images at relatively high speed [8], as only two OCT measurements at each tissue location are required to generate mechanical contrast. This facilitates the application of OCE to surgical scenarios, such as breast-conserving surgery (BCS) [7, 8].

Quantitative micro-elastography (QME) is a variant of compression OCE that incorporates a compliant silicone layer to measure the stress applied across the tissue surface [9, 10]. By assuming a uniaxial stress distribution throughout the tissue and combining the stress measurements at the tissue surface with the strain measurements in the tissue, 3-D maps of the tissue's Young's modulus can be estimated on the micro-scale [9]. QME has recently been demonstrated in a number of applications [11-13]. Our group has primarily focused on developing QME for tumor margin assessment in BCS [14, 15]. Based on the premise that tumors are often stiffer than surrounding benign tissues in breast [16-18], providing surgeons with an intraoperative map of elasticity could help to reduce high re-excision rates (currently 20-30% [19, 20]). To date, QME has been primarily implemented in bulky benchtop setups [14, 15], limiting its compatibility with clinical deployment. To overcome this limitation, we have recently developed a prototype handheld QME probe which holds promise for intraoperative use [21]. In that work, the probe was customized with an annular piezoelectric actuator, providing step-wise mechanical loading to the tissue, demonstrating rapid volumetric QME acquisition and high image contrast between stiff tumor and soft benign tissue regions.

Whilst the piezoelectric actuator provides stable, periodic, mechanical loading, which is important for quasi-static elasticity measurements, there are some drawbacks. Firstly, the piezoelectric actuator complicates the optical and mechanical design of the probe, increasing the complexity and cost of the QME imaging system. For instance, in the handheld QME probe used in [21], to allow the beam to propagate through the annular piezoelectric actuator, the inner and outer diameter of the actuator were customized to be 14 mm and 30 mm, respectively, resulting in a bulky front section of the probe, which may not be compatible with some clinical applications where a compact probe is required. Also, as piezoelectric actuators use delicate materials and additional apparatus, such as a high voltage amplifier, fabricating the actuator and incorporating it in the OCT imaging system can be expensive. Secondly, piezoelectric actuators induce relatively small local strains to the sample. For instance, imparting 1 milli-strain (mε) to a 5 cm thick sample, corresponding to 50 μm stroke from the actuator, requires a 70 mm stack of the piezoelectric material used in [21]. This further complicates the design of the probe and may preclude QME in applications where scans of thick tissue are required. Thirdly, the piezoelectric actuator must be aligned with the optical axis of the scanning beam, to provide mechanical loading perpendicular to the tissue surface. This constrains the front section of the probe to be straight, not suitable to clinical scenarios where complex access to the tissue is required, e.g., in endoscopic applications. In addition, the high driving voltage of the piezoelectric actuator, typically around 150 V, requires extra safety precautions [22] in the design of the probe, introducing more challenges in translating QME to use in the operating room.

To overcome the challenges associated with piezoelectric actuators, several manual loading techniques have recently been proposed [23-25]. The work in [23, 24] demonstrated that 2-D tissue strain and elasticity can be measured, without using an actuator, by manually compressing the imaging probe against the sample. However, this technique is time consuming as several tens or hundreds of B-scans are required to calculate the cumulative strain at the same location. Furthermore, it provides 2-D strain and elasticity maps, limiting its application in scenarios where rapid assessment of a large sample volume is required. Also, instead of using natural motion of the operator's hand, this technique utilizes a semi-freehand setup with a supporting apparatus, limiting its compatibility with clinical scenarios where no supporting apparatus is available. In previous work from our group [25], a finger-mounted variant of QME was demonstrated that also utilized manual compression. However, as no scanning mechanism was incorporated in the imaging system, this method is limited to 1-D measurements. In addition, these previously reported manually-operated techniques compress the tissue continuously in one direction, inducing a large increase in axial strain in the tissue. This can effectively reduce the elasticity sensitivity, due to the nonlinear stress-strain relationship of the tissue.

In this paper, we propose a novel freehand compression-based technique that utilizes a bidirectional manual mechanical loading via the natural motion of the user's hand to enable, for the first time, volumetric manual compression-based QME scans of a $6 \times 6 \times 1$ mm tissue volume in 3.4 seconds. Without using the piezoelectric actuator, the probe design is simplified. The bidirectional loading is important for accurate volumetric measurements, as it limits the range of axial strain imparted to the sample, reducing the impact of nonlinear elasticity that would otherwise cause low elasticity sensitivity. We demonstrate, on a soft silicone phantom with an embedded stiff inclusion, that this technique provides comparable image quality to a mounted benchtop setup using a piezoelectric actuator. In addition, we demonstrate its utility on human breast tissue freshly excised from both mastectomy and BCS (also known as breast wide local excision (WLE)). The OCT and QME results on breast tissue are co-registered with post-operative histology, verifying its capability to distinguish stiff tumor from soft benign tissue.

2 | METHODS

2.1 | Experimental setup

The OCT system is a combination of a commercially available base unit (Thorlabs, Telesto III) and a handheld probe (Thorlabs, OCTH-1300). The light source is a superluminescent diode (SLD) with a central wavelength of 1300 nm and a bandwidth of >170 nm, corresponding to a measured axial resolution of 5.5 µm in air. The measured lateral resolution is 14.4 µm, determined by the probe objective lens (Thorlabs, OCTH-LK30). A plastic ring-style spacer (Thorlabs, OCTH-AIR30) is threaded to the probe and an imaging window (Edmund Optics, VIS-NIR coated fused silica window, #49-642) is attached to the end of the spacer using wax, as displayed in Figure 1(a). We utilize a common-path interferometer, where the reference and sample arms share the same optical path and the surface of the imaging window distal from the probe acts as the reference reflector [26]. A microelectromechanical system (MEMS) scanning mirror is used in the probe to scan the beam over a 6 × 6 mm area. The total C-scan acquisition time is 3.4 seconds for a tissue volume of 6 × 6 × 1 mm. A complementary metal-oxide semiconductor (CMOS) camera is incorporated in the probe to acquire visible-light photographs simultaneously with the OCT scans. The light beams reflected from the reference (the surface of the imaging window distal from the probe) and scattered from the sample are sent back to the spectrometer in the OCT base unit. A computer is used to process the spectra and generate complex OCT signals. A schematic of the setup is shown in Figure 1(b).

To enable QME measurements, we add a silicone bi-layer (see Figure 1(a) inset) between the imaging window and the sample to measure surface stress. As described in previous work [21], the bi-layer comprises two sections: a top, transparent section (Wacker P7676 A and B at 1:1 mixing ratio, ~250 µm thick, local Young's modulus = 18.7 ± 1.2 kPa at 20% axial strain) and a bottom, scattering section (Wacker P7676 A and B at 1:1 mixing ratio, mixed with 0.3 mg/ml TiO_2 scattering particles, ~250 µm thick, local Young's modulus = 18.7 ± 1.2 kPa at 20% axial strain). The two sections are cured together and the large variation in scattering light intensity between the layers results in high OCT contrast that is used to calculate the axial strain of the top section, which is equivalent to the axial strain of the bottom section, as the two sections use the same compound material. This method helps to reduce image artefacts introduced by the edge detection failure due to poor edge contrast at the layer-tissue interface reported in previous work [14]. The scattering bottom section is used to estimate the local strain of the layer between consecutive B-scans, at the measured axial strain [21]. This local strain is then used to calculate the local stress in the sample, knowing the pre-characterized stress-strain curve of the layer material and assuming uniaxial stress distribution throughout the sample. The sample tangent modulus, which is the effective value of Young's modulus at the current state of sample deformation, can be estimated by dividing the layer local stress by the local strain of the sample. We assume that the sample elasticity we measured is in, or near to, a linear region on the stress-strain curve, where tangent modulus is approximately equal to Young's modulus.

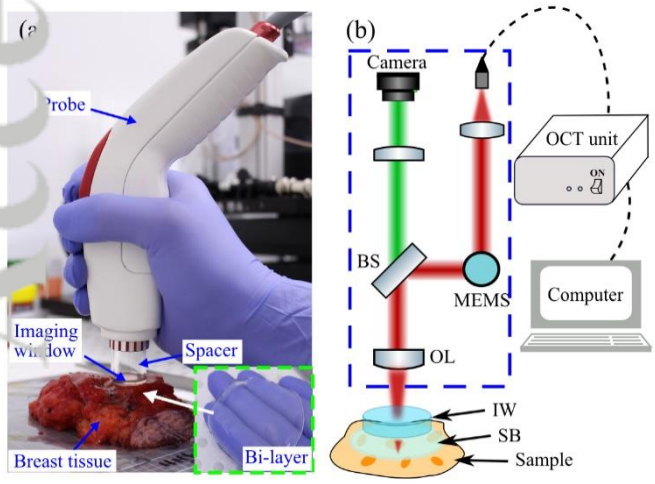

FIGURE 1 (a) Photograph of the probe scanning a breast tissue specimen. Inset, photograph of the bi-layer. (b) Schematic of the optical path and the experimental setup. The blue dashed frame indicates the components inside the probe. BS, beam splitter. MEMS, microelectromechanical system. OL, objective lens. IW, imaging window. SB, silicone bi-layer.

2.2 | Bidirectional manual compression approach

In the absence of a piezoelectric actuator, we create phase difference between corresponding B-scan pairs by manually compressing and decompressing the handheld probe against the layer and the sample. This bidirectional manual compression approach is used to reduce variations in the axial strain, which can lead to variations in the elasticity measurement due to the nonlinear stress-strain relationship of the sample. Figure 2(a) shows a schematic diagram of the axial strain on a homogeneous sample using the bidirectional manual compression approach. In this schematic, the sample is first pre-loaded to a axial strain level of, typically, -0.15. In practice, the user can monitor and estimate the axial strain level via the live view of the OCT B-scans on the computer, where the interface between the two sections of the bi-layer can be clearly identified. When the OCT acquisition starts, the sample is compressed continuously for ~1.7 seconds until another axial strain level of, typically, -0.25, is reached at approximately the halfway point of the C-scan acquisition. The start time and the halfway point of the scan can be indicated, and the scanning location can be monitored, from the trajectory of the scanning beam in the live video acquired using the CMOS camera. Then, the sample is decompressed for ~1.7 seconds during the remainder of the C-scan at approximately the same speed in the opposite direction. In practice, there will be a smooth transition stage between compression and decompression due to viscoelastic response of the sample, as will be illustrated in Section 2.3, instead of the sharp corner displayed in Figure 2(a). In the experiment, the user was trained for ~10 minutes to achieve approximately the right amount of axial strains and to apply a fairly constant rate of compression-decompression during the scan. Figure 2(b) and 2(c) show zoomed-in diagrams illustrating

axial strain in the compression and decompression stages, respectively.

During compression and decompression, the sample is scanned using the custom bidirectional scan pattern, recently introduced by our group [21]. As illustrated in Figure 2(d) and 2(e), which are the *x*-position of the custom bidirectional scan pattern during compression and decompression, respectively, the scan pattern comprises two regions: a linear B-scan region which scans the sample in positive (green lines) and negative (blue lines) *x*-directions, and a sinusoidal turn-around region between consecutive B-scans in opposite directions. The OCT A-scan period used in the scan is 7 µs, corresponding to an A-scan rate of 143 kHz. In our scan pattern, there are 364 A-scans in each of the linear B-scan regions and 364 B-scan locations in a C-scan, resulting in lateral spatial sampling of 16.5 µm in both *x*- and *y*-directions. The frequency of the sinusoidal wave in the turn-around region is 238 Hz, corresponding to 300 A-scan periods in each turn-around region. Combining the linear B-scan regions and the sinusoidal turn-around regions, the effective B-scan rate is 215 Hz. Figure 2(f) and 2(g) show the relative *y*-position of the scanning beam on the sample in the custom bidirectional scan pattern during compression and decompression, respectively. Marked by the same color in green or blue, each B-scan location (*y*-position) is scanned twice by the scanning beam in the same *x*-direction to enable phase difference measurements, and consecutive B-scan locations are scanned in opposite directions. In post-processing, the orientation of every alternate B-scan is reversed to display all the B-scans in the same direction.

In Figure 2(b) and 2(c), the *y*-axes are the axial strain relative to the "0" point in each figure, and the green and blue straight lines indicate the linear B-scan regions in positive and negative B-scan directions, respectively. The difference in axial strain between consecutive B-scans in the same scan direction, here termed 'local strain', is estimated from the phase difference between these B-scans. The local strain is negative in the compression stage (Figure 2(b)), while it is positive in the decompression stage (Figure 2(c)). In an ideal scenario, for a homogeneous sample, the local strain between each B-scan pair remains constant across the entire volumetric scan, e.g. -0.5 mε for each B-scan pair in Figure 2(b) and 0.5 mε for each B-scan pair in Figure 2(c). However, small variations in local strain occur in practice due to the inconsistent speed of the user's hand. In particular, excessive local strain of the sample can cause phase decorrelation in the axial direction, resulting in a bias of the local strain towards zero; while insufficient local strain of the sample (below the strain noise level) can also introduce a local strain estimation around zero, calculated from the phase noise in the strain measurement. The latter scenario happens more frequently at the transition stage between compression and decompression where the speed of the hand motion is relatively low.

2.3 | Elasticity sensitivity

To quantify the performance of our approach, we acquired scans of a homogeneous silicone and calculated elasticity sensitivity [21], which is defined as the standard deviation of

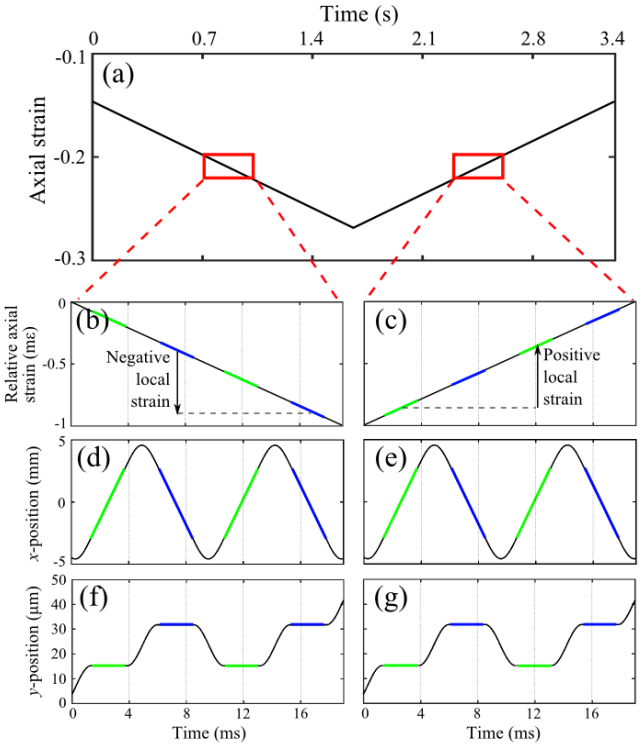

FIGURE 2 Schematic diagrams of the bidirectional manual compression loading mechanism. (a) Diagram of the overall compression and decompression loading. (b) and (c) are the diagrams of the zoomed-in axial strain in the compression and decompression regions, respectively, with the *y*-axis being the axial strain relative to the "0" point in each figure. In (b) and (c), the relative axial strains between B-scans work as local strains (negative local strain during compression and positive local strain during decompression). (d) and (f) are the *x* and relative *y* scanning positions of the B-scans during the compression loading in (b). (e) and (g) are the *x* and relative *y* scanning positions of the B-scans during the decompression loading in (c). The green and blue lines in (b)-(g) indicate the regions of B-scans in positive and negative scan directions, respectively.

the elasticity measurement. The homogeneous phantom was fabricated with the same compound as the silicone layer, providing the same mechanical properties. Three configurations are compared here:

1. When the probe is mounted in a benchtop setup, with a piezoelectric actuator fixed to the probe.
2. When the probe is freely held by the user, without the piezoelectric actuator, using the bidirectional manual compression approach described above.
3. When the probe is freely held by the user, without the piezoelectric actuator, using a monotonic manual compression approach where the phantom is compressed continuously in one direction at approximately the same speed as used in the bidirectional approach.

In each configuration, 364 B-scan pairs (using the custom bidirectional scan pattern illustrated in Figure 2(d) and 2(e)) at the same *y*-position were acquired on the same phantom. In the first configuration, the bi-layer and the phantom were first pre-loaded to a axial strain of ~-0.2, and a small local strain

(referred to as "perturbation strain" in [21]) was induced with an actuator stroke of 6 µm. The same rectangular area of ~800 µm in *x* by ~50 µm in *z*, centered in *x*, was selected ~100 µm below the phantom surface for each B-scan pair. The axial strain was calculated by measuring the average initial and compressed layer thickness of the top section of the bi-layer above the selected rectangular region in each B-scan pair, shown as each data point in Figure 3(a). The average elasticity value was calculated for the same rectangular region on each B-scan pair, plotted as each data point in Figure 3(b). The elasticity sensitivity of the first configuration, σ_E = 0.7 kPa, is calculated as the standard deviation of the mean elasticity measurement, Figure 3(b), over the entire 364 B-scan pairs.

In the bidirectional manual compression configuration, the same rectangular region was selected on each B-scan pair acquired on the same phantom and bi-layer, and the axial strain was measured from the average initial and compressed layer thickness of the top section of the bi-layer above this region, as plotted in Figure 3(c). Note that as the beam was scanning at the same *y*-position, the beam trajectory in live video was not able to indicate the halfway point of the entire 364 B-scan pairs. Instead, the user manually counted 1.7 seconds using a timer while compressing, resulting in an error in estimating the halfway point. In Figure 3(c), the axial strain mostly decreases during compression (negative local strain) for the first 220 B-scan pairs and increases during decompression (positive local strain) for the remaining B-scans, with the maximum and minimum axial strain of -0.17 and -0.26. In addition, the decreasing and increasing slopes of the axial strain are not constant, as expected from the natural motion of the user's hand, resulting in variations in local strain between consecutive B-scans. The average elasticity of the selected region was measured for each B-scan pair, as shown in Figure 3(d). In this figure, the measured elasticity value varies at a low-frequency, as the stress-strain curve of the sample is nonlinear across the axial strain range. The high-frequency fluctuation in the elasticity measurement is likely due to variations in local strain, as the elasticity values are directly related and calculated from the local strain. The artificially high or low elasticity values, e.g., the peaks in red circles and troughs in green circles, respectively, in Figure 3(d), are likely caused by two scenarios: too much hand motion could introduce decorrelation in the phase difference measurement; whilst too little hand motion could introduce a local strain below the strain noise level. In both scenarios, the local strain measurement is purely based on the random strain noise, and this measurement could be artificially high or low. Despite these artefacts in elasticity measurements, the elasticity sensitivity of the bidirectional manual compression configuration was measured to be 2.0 kPa, which is a relatively small value.

To demonstrate the relatively high elasticity sensitivity using the bidirectional manual compression approach, for comparison, Figure 3(e) and 3(f) show the axial strain and elasticity values measured at the same *y*-position using the monotonic manual compression approach. As plotted in Figure 3(e), the axial strain increases continuously as the phantom and bi-layer were compressed continuously in the same direction over the entire 364 B-scan pairs. We note that as it was difficult to control the hand motion to achieve exactly the same compression rate as in Figure 3(c), at the beginning

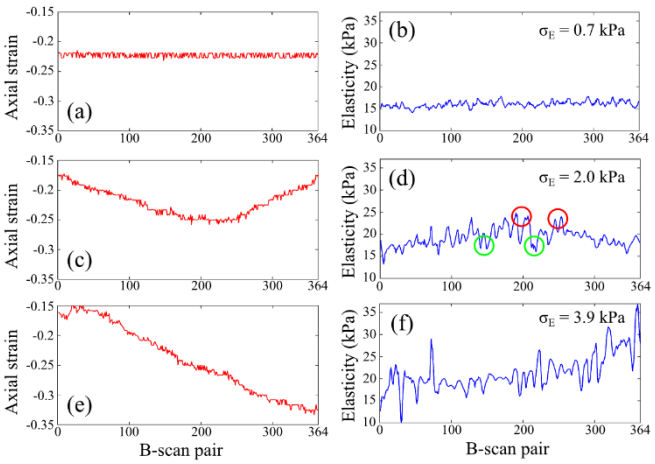

FIGURE 3 Axial strain and elasticity measurements on a homogeneous silicone phantom. (a) and (b), axial strain and elasticity measurement using the mounted setup with a piezoelectric actuator. (c) and (d), axial strain and elasticity measurement using the bidirectional manual compression approach. Red and green circles represent example regions where the elasticity values are artificially high and low, respectively. (e) and (f), axial strain and elasticity measurement using the monotonic manual compression approach. The elasticity sensitivities, σ_E, are displayed in (b), (d) and (f).

of the monotonic compression (approximately the first 80 B-scan pairs in Figure 3(e)), the average slope of the compression was small compared to that at the same region in Figure 3(c), as the manual compression was slightly delayed due to a lag in the response time of the human operator. This results in a large variation in the elasticity measurement due to a low signal-to-noise ratio in the phase difference measurement, a similar artefact to that displayed at the turn-around region in Figure 3(c). Between the 80th and 250th B-scan pairs, the measured elasticity values and standard deviations in Figure 3(d) and 3(f) are similar, due to similar compression rate and axial strain range. However, from the 250th to the last B-scan pair, the measured elasticity values and standard deviations in Figure 3(f) are much higher than that in Figure 3(d), most likely due to the nonlinear stress-strain relationship at the high axial strain range reached by the monotonic compression method. Measured from Figure 3(f), excluding the first 80 B-scan pairs where the elasticity measurement is noisy, the elasticity sensitivity of this monotonic manual compression configuration is 3.9 kPa, much larger than that of the bidirectional compression-decompression approach.

Note that in [21], we characterized elasticity sensitivity using a homogeneous silicone phantom fabricated from a different batch of silicone compound and at a higher pre-load (~-0.3). The measured elasticity sensitivity was 2.2 kPa for the mounted configuration, and 2.6 kPa for the handheld configuration using the piezoelectric actuator, ~20% degraded from the mounted configuration [21]. In comparison, the elasticity sensitivities of the bidirectional and monotonic manual compression approaches described in this paper are, respectively, ~200% and ~460% degraded from the mounted configuration, indicating that the manual compression approaches introduce additional noise in elasticity measurement due to variations in bulk and local strain.

2.4 | Tissue-mimicking phantom and breast tissue specimens

We performed handheld volumetric manual compression-based QME on an inclusion-embedded tissue-mimicking silicone phantom and freshly dissected breast tissue specimens from mastectomy and WLE surgeries. The silicone phantom comprises two parts: a soft base material (Wacker P7676 A and B at 1:1 mixing ratio) and a stiff inclusion (Wacker RT601 A and B and silicone oil (Wacker AK 50) at 10:1:10 mixing ratio). The tangent moduli of the base material and the inclusion were measured to be 18.7 ± 1.2 kPa and 277.0 ± 10.9 kPa, respectively, at 20% axial strain, using a custom uniaxial compression device. To achieve OCT signal-to-noise ratio similar to that in tissue, we added TiO_2 scattering particles (Sigma Aldrich, product 232033, average particle size of 1 µm) in both the base material (mixing concentration = 1 mg/ml) and the inclusion (mixing concentration = 3 mg/ml). In addition, 11 specimens of freshly excised human breast tissue were scanned: 5 mastectomy and 6 WLE specimens. A tissue sample with a size of ~4 × 36 × 5 mm was dissected from each mastectomy specimen and scanned within one hour of excision, whilst the WLE specimens remained intact (typical volume of ~50 × 50 × 20 mm) and were imaged in the same timeframe. Following the scans, each mastectomy tissue sample was bisected and placed in two cassettes to enable preparation for histology in the same plane as the *en face* plane of the QME scans. For WLE specimens, the histology was prepared following the standard histological procedure used at Fiona Stanley Hospital, where each specimen was sliced in a "bread-loaf" fashion from the lateral to medial margin, in the same plane as OCT/QME B-scans [15]. The histology was acquired ~1 week after the scan of each specimen. Specimens were obtained from patients undergoing surgery at Fiona Stanley Hospital, Western Australia (Project No: FSH-2015-032). Informed consent was acquired from each of the patients before the surgery. The ethics for this research project was approved by the Sir Charles Gairdner and Osborne Park Health Care Group Human Research Ethics Committee, Western Australia (HREC No: 2007-152).

2.5 | Signal processing

The signal processing used in this study is largely the same as that described in [21]. Both the complex weighted phase difference and local strain maps were smoothed using a 2-D Gaussian filter with FWHM of 30 µm in the same plane as the OCT B-scan. The 3-D micro-elastograms were smoothed by a median filter covering 45 µm in both *x*- and *y*-directions. Matlab R2016a was used to process the data on a system with two Intel Xeon E5-2690 8-core CPUs, 192 GB of RAM, and a 1 TB solid-state drive. The total processing time from raw OCT data to 3-D micro-elastograms for a sample volume of 6 × 6 × 1 mm is ~20 minutes.

3 | RESULTS

3.1 | Handheld volumetric manual compression-based QME on the tissue-mimicking phantom

We scanned the tissue-mimicking phantom using the mounted configuration with the piezoelectric actuator (Configuration 1 in Section 2.3) and the freehand configuration with the bidirectional manual compression approach (Configuration 2 in Section 2.3) and compared the image quality. Figure 4(a) and 4(b) show the *en face* OCT image and *en face* micro-elastogram acquired using the mounted configuration, setting a benchmark for image quality. The images are shown at a depth of ~500 µm below the phantom surface, with the horizontal axis being the OCT B-scan direction. The stiff inclusion, with the mean elasticity value and standard deviation measured to be 370.4 ± 94.7 kPa, can be clearly delineated in both the OCT image and micro-elastogram. The elasticity values of the base material are also calculated, with 20.8 ± 3.8 kPa and 24.2 ± 4.1 kPa for the rectangular regions inside the red and black dashed frames, respectively, in Figure 4(b). The consistent elasticity values in the two rectangular regions indicate that the base material of the phantom was fairly uniformly compressed in the mounted setup. Figure 4(c) is an elasticity profile along the dashed horizontal line across the inclusion in Figure 4(b). Figure 4(d) and 4(e) show the *en*

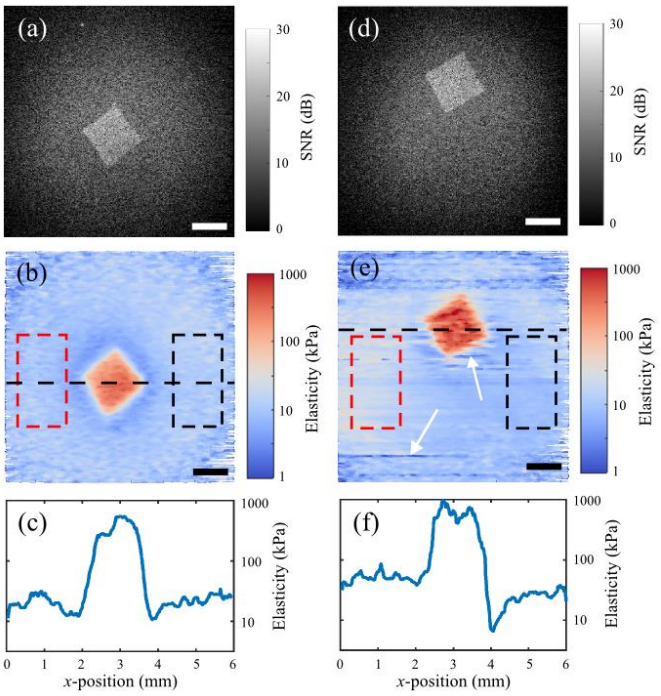

FIGURE 4 (a), (b) *En face* OCT image and micro-elastogram of the tissue-mimicking phantom acquired with the mounted setup. (c) Elasticity profile along the dashed horizontal line in (b). (d), (e) *En face* OCT image and micro-elastogram of the same phantom acquired with the handheld probe using the freehand bidirectional manual compression approach. The white arrows in (e) indicate the band artefacts in the micro-elastogram. (f) Elasticity profile along the dashed horizontal line in (e). Scale bars = 1 mm.

face OCT image and *en face* micro-elastogram acquired using the freehand bidirectional manual compression approach, also at an imaging depth of ~500 µm and with the horizontal axis being the OCT B-scan direction. The inclusion can be clearly delineated in the OCT image, suggesting negligible effect of lateral hand motion on OCT image quality. In the micro-elastogram, Figure 4(e), the inclusion is also clearly visible and can be easily distinguished from the soft base material. The measured elasticity value of the inclusion region is 517.2 ± 193.1 kPa, approximately 1.4 times larger than that measured in Figure 4(b), most likely due to the higher preload on the phantom in the freehand configuration. There are some distortions and image artefacts in Figure 4(e), e.g., the horizontal bands indicated by the white arrows, caused by hand motion in both lateral and axial directions. In addition, the elasticity values of the base material are calculated to be 39.5 ± 9.4 kPa and 20.2 ± 4.4 kPa for the rectangular regions inside the red and black dashed frames, respectively. From this measurement, the left-hand side of the micro-elastogram displays higher elasticity for the base material than the right-hand side, likely due to a small tilt of the probe during the manual compression scan. In the black dashed frame in Figure 4(e), the top section displays slightly higher elasticity values than the bottom section, most likely due to the axial strain variations at different B-scan locations caused by the hand motion. Despite these artefacts, the overall image quality in micro-elastogram Figure 4(e) is comparable to that in Figure 4(b). Figure 4(f) is an elasticity profile along the dashed horizontal line across the inclusion in Figure 4(e). The measured inclusion elasticity in Figure 4(f) is slightly higher than that in Figure 4(c), most likely due to the slightly different preloads in these two scan configurations. The difference in the measured elasticity of the base material between the left- and right-hand sides is also clearly presented in Figure 4(f), due to the tilt of the handheld probe during the manual compression scan.

3.2 | Handheld volumetric manual compression-based QME on human breast tissues

To verify the results acquired on breast tissues, we also scanned the specimens with a wide-field, benchtop QME system described previously [14] prior to performing the handheld volumetric manual-compression scans. This allowed us to co-register photographs, OCT images and micro-elastograms, acquired in both the freehand and the wide-field benchtop scans, with post-operative histology. Among these scanned tissues, according to post-operative histology, invasive cancer was reported in 4 dissected mastectomy specimens, and no cancer was found within 5 mm deep from the scanned surface of the WLE specimens. In this section, we present representative results from 2 mastectomy specimens and 1 WLE specimen.

Figure 5 shows the wide-field, benchtop QME scan and the handheld volumetric manual compression-based QME scan of a mastectomy specimen. Figure 5(a) is a mosaicked photograph acquired by the wide-field, benchtop QME system, with a field-of-view of 46 × 46 mm. Figure 5(b) is a wide-field overlaid *en face* OCT/micro-elastogram image, displayed at ~300 µm below the tissue surface. In Figure 5(b), adipose tissue and milli-scale non-contact regions are segmented using a custom, thresholding-based algorithm [8]. Figure 5(c) is the histology of the scanned tissue surface. Figure 5(d) is the photograph acquired using the handheld probe, at the location indicated by the green frame in Figure 5(a). Figure 5(e) and 5(f) are *en face* OCT image and *en face* micro-elastogram, respectively, acquired using the freehand manual compression approach at the same location indicated by the green frame in Figure 5(b). In Figure 5(e), the adipose tissue can be readily identified owing to its characteristic honeycomb structure [7, 8, 14]. In Figure 5(f), low elasticity values were measured for the adipose tissue regions, and the neighboring areas displaying high elasticity values are tumor regions with invasive ductal carcinoma (IDC), confirmed by the histology, Figure 5(g), which is the zoomed-in image of the green frame in Figure 5(c). Representative regions of IDC and adipose tissue are selected by the black and red dashed frames in Figure 5(f), with the measured elasticity values of 383.5 ± 197.1 kPa and 14.8 ± 6.4 kPa, respectively. In this measurement, the elasticity value of IDC is approximately 26 times higher than that of adipose tissue.

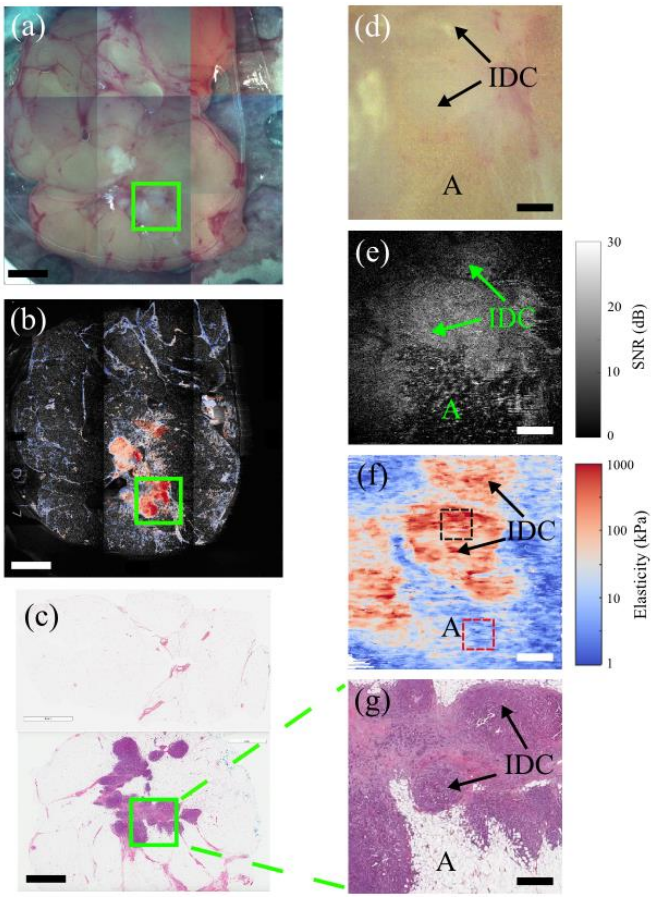

FIGURE 5 Tissue results from mastectomy specimen 1. (a)-(c), wide-field photograph, overlaid *en face* OCT/micro-elastogram and histology. (d) photograph, (e) *en face* OCT and (f) *en face* micro-elastogram acquired using the freehand manual compression approach. (g), zoomed-in histology at the same location as the freehand scan. A, adipose tissue. IDC, invasive ductal carcinoma. Scale bars in (a)-(c) = 6 mm, scale bars in (d)-(g) = 1 mm.

Figure 6 presents the results of handheld volumetric manual compression-based QME on a second mastectomy specimen. Figure 6(a)-6(c) show the wide-field photograph, overlaid *en face* OCT/micro-elastogram image and the histology image, respectively. The overlaid OCT/micro-elastogram image and the histology are displayed at an imaging depth of ~300 μm below the tissue surface. As the size of this specimen was slightly too large to fit into two histology cassettes, it was dissected and prepared in three cassettes instead. Note that the wide-field histology, Figure 6(c), is slightly rotated compared to the wide-field photograph and OCT/micro-elastogram overlay, Figure 6(a) and 6(b), as the orientation and shape of the specimen were altered during the histological processing. Figure 6(d)-6(f) show the photograph, *en face* OCT image and *en face* micro-elastogram, respectively, acquired using the handheld volumetric manual compression-based QME probe. The freehand scan region was co-registered with the wide-field images, indicated by the green frames in Figure 6(a) and 6(b), respectively. In Figure 6(e), the adipose tissue can be clearly distinguished due to its characteristic honeycomb structure, corresponding to a region of low elasticity in Figure 6(f). The regions of denser tissue in Figure 6(e) display high elasticity values in Figure 6(f), corresponding to a region of ductal carcinoma *in situ* (DCIS), confirmed by histology, Figure 6(g), which is the zoomed-in image of the green square frame in Figure 6(c), representing the freehand scan location. Representative regions of DCIS and adipose tissue are selected by the black and red dashed frames in Figure 6(f), with the measured elasticity value of 482.3 ± 297.8 kPa and 20.2 ± 11.5 kPa, respectively. In this measurement, the elasticity value of DCIS is approximately 24 times higher than that of adipose tissue. The measured elasticity values of tumor and adipose tissue regions are higher than that in Figure 5(f). The ratios between the tumor and adipose tissue elasticity values are very similar in Figure 5(f) and 6(f).

As identification of tumor margins during WLE is one potential clinical use of handheld volumetric manual compression-based QME, it is important to also demonstrate its performance on these specimens. Figure 7 presents results from a ~20-mm thick WLE specimen, co-registered with wide-field scans and histology. Figure 7(a) and 7(b) show the wide-field photograph and overlaid *en face* OCT/micro-elastogram image, at an imaging depth of ~300 μm below the tissue surface, on the superficial margin of the specimen. Figure 7(c) is the histology image acquired on the tissue slice orthogonal to the scanned tissue surface. The tissue slice location was co-registered with wide-field, benchtop scans, following the method described in detail in [27], and is indicated by the red dotted line in Figure 7(b). Figure 7(d)-7(f) are the photograph, *en face* OCT image and *en face* micro-elastogram acquired using the handheld volumetric manual compression-based QME probe. The region scanned with the probe is marked by the green frames in the wide-field images, Figure 7(a) and 7(b). The red dotted lines in Figure 7(e) and 7(f) indicate the approximate location of the histology slice presented in the inset of Figure 7(c), which is an estimation of the tissue cross-section scanned with the handheld probe. In Figure 7(e), adipose tissue can be easily distinguished due to its characteristic honeycomb structure,

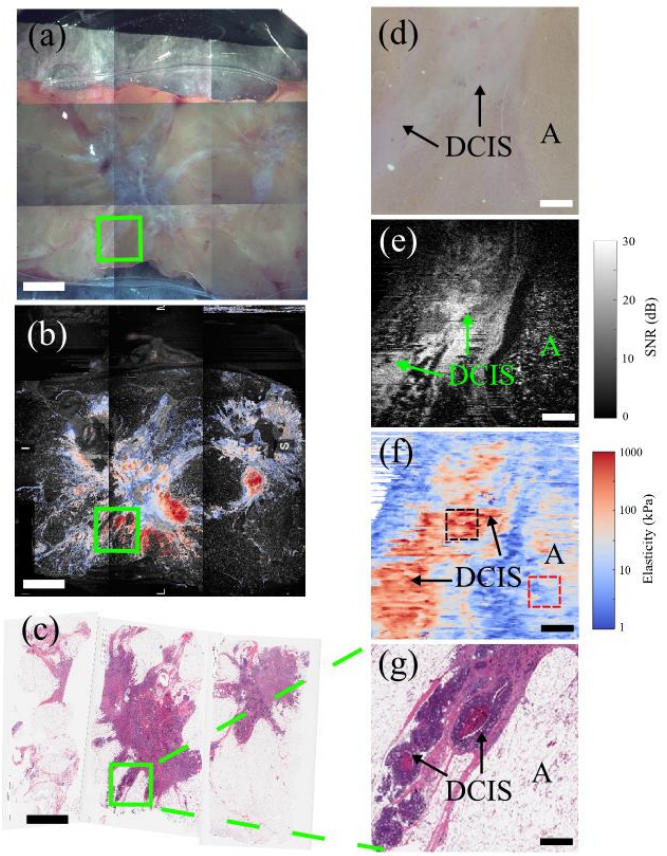

FIGURE 6 Tissue results from mastectomy specimen 2. (a)-(c), wide-field photograph, overlaid *en face* OCT/micro-elastogram and histology. (d) photograph, (e) *en face* OCT and (f) *en face* micro-elastogram acquired using the freehand manual compression approach. (g), zoomed-in histology on the same location as the freehand scan. A, adipose tissue. DCIS, ductal carcinoma *in situ*. Scale bars in (a)-(c) = 6 mm, scale bars in (d)-(g) = 1 mm.

and neighboring fibrous tissue presents relatively homogeneous features in the OCT image. In Figure 7(f), representative regions of fibrous tissue and adipose tissue are selected by the black and red dashed frames, with the measured elasticity value of 53.8 ± 16.7 kPa and 12.6 ± 7.4 kPa, respectively. The fibrous tissue presents higher elasticity than the surrounding adipose tissue, yet relatively low when compared to the elasticity in the tumor regions in Figure 5(f) and 6(f), as expected from previous QME studies [14, 15]. The measured elasticity values of IDC, DCIS and benign tissues shown in our results are also consistent with previous study using an OCT-elastography-based optical biopsy technique [28].

4 | DISCUSSION

We have demonstrated the first handheld volumetric manual compression-based QME, capable of producing comparable OCT and micro-elastogram image quality to that of an actuator-based technique. As we continue to develop QME for clinical use, such as intraoperative imaging in BCS, where

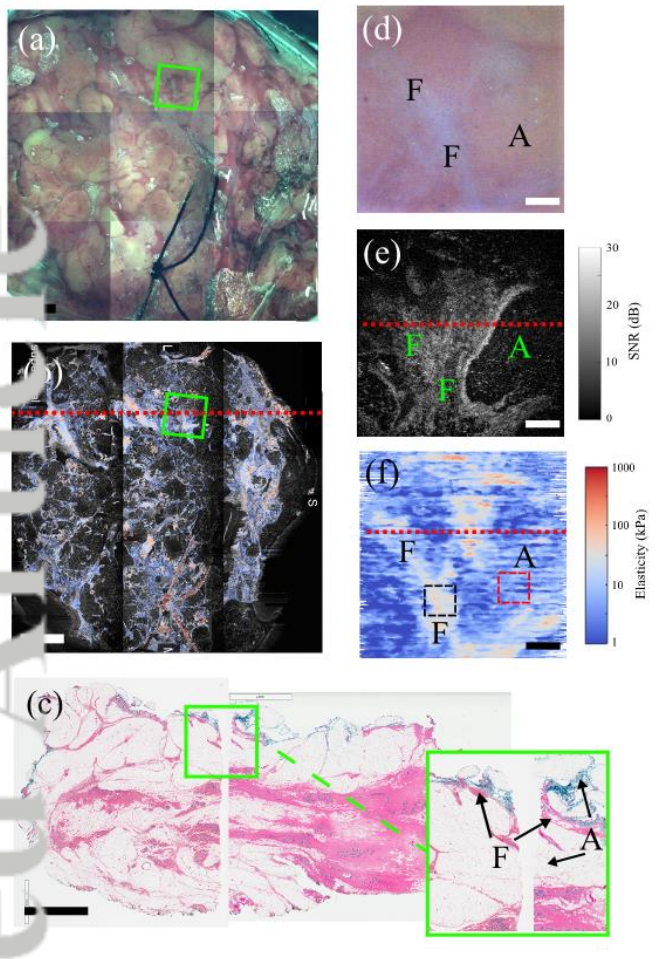

FIGURE 7 Tissue results from a WLE specimen. (a) and (b), wide-field photograph and overlaid *en face* OCT/micro-elastogram image. (c), histology of the tissue slice orthogonal to the scanned surface, with the slice location indicated by the red dotted line in (b). (d) photograph, (e) *en face* OCT and (f) *en face* micro-elastogram acquired using the freehand manual compression approach, with the scanning location indicated by the green frames in (a) and (b). The red dotted lines in (e) and (f) indicate a representative location of the inset in the histology image (c). A, adipose tissue. F, fibrous tissue. Scale bars in (a)-(c) = 6 mm, scale bars in (d)-(f) = 1 mm.

limited space is available in the operating room, our approach may be preferable as no additional equipment is required to apply local strain to the tissue and the simple probe design can more easily incorporate QME scans in the existing surgical protocol, with only marginal sacrifice to OCT and micro-elastogram image quality. In addition, the rapid acquisition guarantees that our technique is compatible with the current timeframe of BCS.

As has been demonstrated in both the phantom and tissue results, our technique provides measurements over a relatively large range of elasticity values (~2 kPa - ~800 kPa, a factor of ~400), realized by the QME method where elasticity is calculated from dividing stress by strain. Typically, the noise level of the strain measurement in our system is tens of με, and the maximum measurable strain value is a few mε before phase decorrelation occurs. In addition, the measurable stress range is from a few Pa to a few hundred Pa, varying by a factor of ~50 - 100. This results in a large measurable range of elasticity, up to a factor of 2000-5000. For instance, in Figure 5(f), the stress in the region of IDC is ~100 Pa and is ~5 Pa in the region of adipose tissue, calculated from the axial and local strain measurement of the silicone bi-layer. In addition, the measured strain of the adipose tissue region is ~20 times higher than that of the IDC region, which is well within the measurable strain range of our system. This results in a range of ~400 times measured for the tissue elasticity.

A limitation of our approach is the requirement to continuously vary the axial strain during the scan, resulting in measuring the elasticity over a nonlinear range in the sample's stress-strain curve, as demonstrated from the silicone phantom scans in Section 2.3. Although this effect appears to be quite small in the silicone and breast samples scanned here, it may be worse in more nonlinear tissues, such as in some breast cancer samples, where the tangent modulus has been reported to vary up to a factor of 3 in an axial strain range of 2.5% [29]. To reduce the axial strain range during the scan in such cases, it may be required to modify the compression to have multiple, smaller compression-decompression cycles to ensure that the tangent modulus is measured in a relatively linear region of the sample's stress-strain curve. In addition, from the phantom measurement displayed in Figure 3(d), there is no evident hysteresis, as the measured elasticity values are similar for the compression and decompression stages. From the tissue results presented in Figure 5(f), 6(f) and 7(f), we have not seen obvious hysteresis, which is consistent with the experimental results described in [29]. However, it is difficult to examine the hysteresis effect in our handheld volumetric manual compression-based QME, as different tissue regions are scanned during the compression and decompression stages. In future work, to measure this hysteresis effect of different tissue types, we can perform compression and decompression scans on the same tissue location and compare the elasticity values acquired at different stages.

Another issue is the difficulty to maintain a constant speed of the hand motion at the compression and decompression stages, resulting in variations in the phase difference measurement which is used to estimate the local strain. Large variations in phase difference measurement can introduce image artefacts in the micro-elastograms, due to phase decorrelation (too much displacement between consecutive B-scans) or low phase difference below the noise level (too small displacement between consecutive B-scans). Particularly, at the transition stage between compression and decompression, the displacement between consecutive B-scans can be very small, resulting in low local strain signal-to-noise ratio and, consequently, low sensitivity in the elasticity measurement. This issue will become more prominent when translating our approach to *in vivo* imaging in the operating room, where it is more difficult to maintain the constant compression due to complex tissue structure and involuntary motion of the patient. To mitigate this issue and improve the image quality, faster acquisition methods, e.g. Fourier domain mode-locked swept source laser [30, 31], can be used, and averaging of multiple B-scans at the same location can help to improve the elasticity sensitivity.

In our demonstration of handheld volumetric manual compression-based QME, the total scan time for a 6 × 6 × 1 mm tissue volume is 3.4 seconds. Approximately the

first half of the volume is acquired during the compression stage, and the second half of the volume is acquired during the decompression stage. However, it is difficult to control the hand motion to compress the tissue for exactly 1.7 seconds and decompress for the other 1.7 seconds. In addition, it takes ~200-300 milliseconds for the tissue to transition from compression to decompression, due to the viscoelastic responses of the tissue and the silicone layer, as well as the response time for a human operator to change the direction of the hand motion. To minimize the timing error and to avoid scanning during the transition stage, one potential method is to customize the scan pattern of the MEMS mirror: the first half C-scan is acquired for 1.7 seconds, while the tissue is compressed; then the MEMS mirror is held steady for ~500 milliseconds, to allow reversing the compression direction; then the second half C-scan is acquired for 1.7 seconds, while the tissue is decompressed.

We have demonstrated that handheld volumetric manual compression-based QME is capable of scanning tissues with relatively flat surfaces, e.g., the dissected mastectomy specimens in this study. However, for tissues with complex structures, e.g., uneven or slippery surfaces, the manual compression approach might not be suitable, due to phase decorrelation caused by relatively large lateral movement between the probe and the tissue. To address this issue, a smaller imaging window can be used to compress the tissue more locally. In this case, the relatively small tissue surface contacting the imaging window can be considered flat. In addition, the indentation of the tissue caused by the small diameter of the imaging window helps increase the friction between the probe and the tissue, restricting the lateral motion of the probe during the scan.

In this study, 11 excised tissue specimens (5 mastectomies and 6 WLEs) were scanned using handheld volumetric manual compression-based QME. However, a larger sample size is needed to determine the diagnostic accuracy, i.e., the sensitivity and specificity, in identifying tumor and benign tissue. In addition to margin assessment on the excised specimen during BCS, this technique could be implemented *in vivo* to help surgeons detect residual tumor in the surgical cavity. To achieve this, some modifications to the form factor of the probe are required to make it more accessible to breast cavities. In addition, the probe can be designed to fit in other surgical applications, e.g., lung cancer and liver cancer surgeries.

5 | CONCLUSION

In this paper, we have demonstrated a freehand volumetric manual compression-based QME approach, providing rapid scans of a 6 × 6 × 1 mm tissue volume in 3.4 seconds. The elasticity sensitivity of this approach was characterized and compared to a bench-mounted QME setup using a piezoelectric actuator and a freehand setup using a monotonic manual compression approach. We performed handheld volumetric manual compression-based QME on a structured silicone phantom, demonstrating comparable image quality to the mounted scan using a piezoelectric actuator. We also used our approach to scan 11 freshly excised human breast specimens from both mastectomy and WLE procedures, and co-registered the photograph, OCT images and micro-elastograms with histology, demonstrating that tumor can be distinguished from the surrounding benign tissue based on elevated elasticity.

ACKNOWLEDGMENTS

This research was supported by grants and fellowships from the Australian Research Council, the National Health and Medical Research Council (Australia), the National Breast Cancer Foundation (Australia), the Department of Health, Western Australia, the Cancer Council, Western Australia, and through a research contract with OncoRes Medical, Australia.

CONFLICT OF INTEREST

B.F.K receives research funding from OncoRes Medical, Australia. B.F.K, L.C, A.C, B.L and C.M.S are shareholders of OncoRes Medical, Australia. The other authors declare that there are no conflicts of interest related to this article.

REFERENCES

[1] B. F. Kennedy, K. M. Kennedy, and D. D. Sampson, "A Review of Optical Coherence Elastography: Fundamentals, Techniques and Prospects," *IEEE J. Sel. Top. Quantum Electron* **2014**, *20*, 7101217.

[2] K. V. Larin and D. D. Sampson, "Optical coherence elastography - OCT at work in tissue biomechanics [Invited]," *Biomed. Opt. Express* **2017**, *8*, 1172.

[3] D. Huang, E. A. Swanson, C. P. Lin, J. S. Schuman, W. G. Stinson, W. Chang, M. R. Hee, T. Flotte, K. Gregory, C. A. Puliafito, and J. G. Fujimoto, "Optical coherence tomography," *Science* **1991**, *254*, 1178.

[4] J. G. Fujimoto, C. Pitris, S. A. Boppart, and M. E. Brezinski, "Optical coherence tomography: an emerging technology for biomedical imaging and optical biopsy," *Neoplasia (New York, N.Y.)* **2000**, *2*, 9.

[5] B. F. Kennedy, P. Wijesinghe, and D. D. Sampson, "The emergence of optical elastography in biomedicine," *Nat. Photonics* **2017**, *11*, 215.

[6] B. F. Kennedy, S. H. Koh, R. A. McLaughlin, K. M. Kennedy, P. R. T. Munro, and D. D. Sampson, "Strain estimation in phase-sensitive optical coherence elastography," *Biomed. Opt. Express* **2012**, *3*, 1865.

[7] B. F. Kennedy, R. A. McLaughlin, K. M. Kennedy, L. Chin, P. Wijesinghe, A. Curatolo, A. Tien, M. Ronald, B. Latham, C. M. Saunders, and D. D. Sampson, "Investigation of Optical Coherence Microelastography as a Method to Visualize Cancers in Human Breast Tissue," *Cancer Res* **2015**, *75*, 3236.

[8] W. M. Allen, L. Chin, P. Wijesinghe, R. W. Kirk, B. Latham, D. D. Sampson, C. M. Saunders, and B. F. Kennedy, "Wide-field optical coherence micro-elastography for intraoperative assessment of human breast cancer margins," *Biomed. Opt. Express* **2016**, *7*, 4139.

[9] K. M. Kennedy, L. Chin, R. A. McLaughlin, B. Latham, C. M. Saunders, D. D. Sampson, and B. F. Kennedy, "Quantitative micro-elastography: imaging of tissue elasticity using compression optical coherence elastography," *Sci. Rep.* **2015**, *5*, 15538.

[10] K. M. Kennedy, S. Es'haghian, L. Chin, R. A. McLaughlin, D. D. Sampson, and B. F. Kennedy, "Optical palpation: optical coherence tomography-based tactile imaging using a compliant sensor," *Opt. Lett.* **2014**, *39*, 3014.

[11] S. Es'haghian, K. M. Kennedy, P. Gong, Q. Li, L. Chin, P. Wijesinghe, D. D. Sampson, R. A. McLaughlin, and B. F. Kennedy, "In vivo volumetric quantitative micro-elastography of human skin," *Biomed. Opt. Express* **2017**, *8*, 2458.

[12] Q. Fang, A. Curatolo, P. Wijesinghe, Y. L. Yeow, J. Hamzah, P. B. Noble, K. Karnowski, D. D. Sampson, R. Ganss, J. K. Kim, W. M. Lee, and B. F. Kennedy, "Ultrahigh-resolution optical coherence

elastography through a micro-endoscope: towards in vivo imaging of cellular-scale mechanics," *Biomed. Opt. Express* **2017**, *8*, 5127.

[13] P. Wijesinghe, N. J. Johansen, A. Curatolo, D. D. Sampson, R. Ganss, and B. F. Kennedy, "Ultrahigh-Resolution Optical Coherence Elastography Images Cellular-Scale Stiffness of Mouse Aorta," *Biophys. J.* **2017**, *113*, 2540.

[14] W. M. Allen, K. M. Kennedy, Q. Fang, L. Chin, A. Curatolo, L. Watts, R. Zilkens, S. L. Chin, B. F. Dessauvagie, B. Latham, C. M. Saunders, and B. F. Kennedy, "Wide-field quantitative micro-elastography of human breast tissue," *Biomed. Opt. Express* **2018**, *9*, 1082.

[15] K. M. Kennedy, R. Zilkens, W. M. Allen, K. Y. Foo, Q. Fang, L. Chin, R. W. Sanderson, J. D. Anstie, P. Wijesinghe, A. Curatolo, H. E.I. Tan, N. Morin, B. Kunjuraman, C. Yeomans, S. L. Chin, H. DeJong, K. Giles, B. F. Dessauvagie, B. Latham, C. M. Saunders, and B. F. Kennedy, "Diagnostic accuracy of quantitative micro-elastography for margin assessment in breast- conserving surgery," *Submitted to Cancer Res.* **2019**.

[16] A. L. McKnight, J. L. Kugel, P. J. Rossman, A. Manduca, L. C. Hartmann, and R. L. Ehman, "MR Elastography of Breast Cancer: Preliminary Results," *Am. J. Roentgenol.* **2002**, *178*, 1411.

[17] A. Evans, P. Whelehan, K. Thomson, D. McLean, K. Brauer, C. Purdie, L. Baker, L. Jordan, P. Rauchhaus, and A. Thompson, "Invasive Breast Cancer: Relationship between Shear-wave Elastographic Findings and Histologic Prognostic Factors," *Radiology* **2012**, *263*, 673.

[18] J. M. Chang, I. A. Park, S. H. Lee, W. H. Kim, M. S. Bae, H. R. Koo, A. Yi, S. J. Kim, N. Cho, and W. K. Moon, "Stiffness of tumours measured by shear-wave elastography correlated with subtypes of breast cancer," *Eur. Radiol.* **2013**, *23*, 2450.

[19] H. Ballal, D. B. Taylor, A. G. Bourke, B. Latham, and C. M. Saunders, "Predictors of re-excision in wire-guided wide local excision for early breast cancer: a Western Australian multi-centre experience," *ANZ J. Surg.* **2015**, *85*, 540.

[20] R. Jeevan, D. A. Cromwell, M. Trivella, G. Lawrence, O. Kearins, J. Pereira, C. Sheppard, C. M. Caddy, and J. H. P. van der Meulen, "Reoperation rates after breast conserving surgery for breast cancer among women in England: retrospective study of hospital episode statistics," *BMJ* **2012**, *345*, 1.

[21] Q. Fang, B. Krajancich, L. Chin, R. Zilkens, A. Curatolo, L. Frewer, J. D. Anstie, P. Wijesinghe, C. Hall, B. F. Dessauvagie, B. Latham, C. M. Saunders, and B. F. Kennedy, "Handheld probe for quantitative micro-elastography," *Biomed. Opt. Express* **2019**, *10*, 4034.

[22] IEC 60601-1-11:2015 - Medical electrical equipment (2nd Edition.), Available: https://www.iso.org/standard/65529.html **2015**.

[23] A. A. Sovetsky, A. L. Matveyev, L. A. Matveev, D. V. Shabanov, and V. Y. Zaitsev, "Manually-operated compressional optical coherence elastography with effective aperiodic averaging: demonstrations for corneal and cartilaginous tissues," *Laser Phys. Lett.* **2018**, *15*, 085602.

[24] V. Y. Zaitsev, A. L. Matveyev, L. A. Matveev, G. V. Gelikonov, E. V. Gubarkova, N. D. Gladkova, and A. Vitkin, "Hybrid method of strain estimation in optical coherence elastography using combined sub-wavelength phase measurements and supra-pixel displacement tracking," *J. Biophotonics* **2016**, *9*, 499.

[25] R. W. Sanderson, A. Curatolo, P. Wijesinghe, L. Chin, and B. F. Kennedy, "Finger-mounted quantitative micro-elastography," *Biomed. Opt. Express* **2019**, *10*, 1760.

[26] B. F. Kennedy, R. A. McLaughlin, K. M. Kennedy, L. Chin, A. Curatolo, A. Tien, B. Latham, C. M. Saunders, and D. D. Sampson, "Optical coherence micro-elastography: mechanical-contrast imaging of tissue microstructure," *Biomed. Opt. Express* **2014**, *5*, 2113.

[27] W. M. Allen, K. Y. Foo, R. Zilkens, K. M. Kennedy, Q. Fang, L. Chin, B. F. Dessauvagie, B. Latham, C. M. Saunders, and B. F. Kennedy, "Clinical feasibility of optical coherence micro-elastography for imaging tumor margins in breast-conserving surgery," *Biomed. Opt. Express* **2018**, *9*, 6331.

[28] E. V. Gubarkova, A. A. Sovetsky, V. Y. Zaitsev, A. L. Matveyev, D. A. Vorontsov, M. A. Sirotkina, L. A. Matveev, A. A. Plekhanov, N. P. Pavlova, S. S. Kuznetsov, A. Y. Vorontsov, E. V. Zagaynova, and N. D. Gladkova, "OCT-elastography-based optical biopsy for breast cancer delineation and express assessment of morphological/molecular subtypes," *Biomed. Opt. Express* **2019**, *10*, 2244.

[29] V. Y. Zaitsev, A. L. Matveyev, L. A. Matveev, E. V. Gubarkova, A. A. Sovetsky, M. A. Sirotkina, G. V. Gelikonov, E. V. Zagaynova, N. D. Gladkova, and A. Vitkin, "Practical obstacles and their mitigation strategies in compression optical coherence elastography of biological tissues," *J. Innov. Opt. Heal. Sci.* **2017**, *10*, 1742006.

[30] J. P. Kolb, T. Pfeiffer, M. Eibl, H. Hakert, and R. Huber, "High-resolution retinal swept source optical coherence tomography with an ultra-wideband Fourier-domain mode-locked laser at MHz A-scan rates," *Biomed. Opt. Express* **2017**, *9*, 120.

[31] M. Singh, C. Wu, C. H. Liu, J. Li, A. Schill, A. Nair, and K. V. Larin, "Phase-sensitive optical coherence elastography at 1.5 million A-Lines per second," *Opt. Lett.* **2015**, *40*, 2588.